

Received June 23, 2020, accepted July 1, 2020, date of publication July 3, 2020, date of current version July 15, 2020.

Digital Object Identifier 10.1109/ACCESS.2020.3007024

3D Reconstruction for Super-Resolution CT Images in the Internet of Health Things Using Deep Learning

JING ZHANG¹, LING-RUI GONG², KEPING YU^{3,4}, (Member, IEEE),
XIN QI³, (Member, IEEE), ZHENG WEN⁵, (Member, IEEE), QIAOZHI HUA⁶,
AND SAN HLAING MYINT³

¹Department of Computer Science and Technology, Xi'an University of Science and Technology, Xi'an 710054, China

²Department of Information Science and Technology, Northwest University, Xi'an 710127, China

³Global Information and Telecommunication Institute, Waseda University, Tokyo 169-8050, Japan

⁴Shenzhen Boyi Technology Company Ltd., Shenzhen 518125, China

⁵School of Fundamental Science and Engineering, Waseda University, Tokyo 169-8050, Japan

⁶Computer School, Hubei University of Arts and Science, Xiangyang 441000, China

Corresponding authors: Qiaozhi Hua (11722@hbuas.edu.cn) and Keping Yu (keping.yu@aoni.waseda.jp)

This work was supported in part by the National Natural Science Foundation of China under Grant 61902311, in part by the Postdoctoral Research Foundation of China under Grant 2019M663801, in part by the Natural Science Foundation of Shaanxi Province under Grant 2019JM-348 and Grant 2019KRM021, in part by the Scientific Research Plan of Shaanxi Provincial Education Department under Grant 19JK0541, and in part by the Japan Society for the Promotion of Science (JSPS) Grants-in-Aid for Scientific Research (KAKENHI) under Grant JP18K18044.

ABSTRACT The Internet of Health Things (IoHT) enables health devices to connect to the Internet and communicate with each other, which provides the high-accuracy and high-security diagnosis result in the medical area. As essential parts of the IoHT, computed tomography (CT) images help doctors diagnose disease. In the traditional disease diagnosing process, low-resolution medical CT images produce low-accuracy diagnosis results for microlesions. Moreover, CT images can only provide 2D information about organs, and doctors should estimate the 3D shape of a lesion based on experience. To solve these problems, we propose a 3D reconstruction method for secure super-resolution computed tomography (SRCT) images in the IoHT using deep learning. First, we use deep learning to obtain secure SRCT images from low-resolution images in the IoHT. To this end, we adopt a conditional generative adversarial network (CGAN) based on the edge detection loss function (EDLF) in the deep learning process, namely EDLF-CGAN algorithm. In this algorithm, the CGAN is employed to generate SRCT images with luminance and contrast as the input auxiliary conditions, which can improve the accuracy of super-resolution (SR) images. An EDLF is proposed to consider the edge features in the generated SRCT images, which reduces the deformation of generated image. Second, we apply the secure SR images generated from the deep learning method to perform 3D reconstruction. An advanced ray casting 3D reconstruction algorithm that can reduce the number of rays by selecting the appropriate bounding box is proposed. Compared with the traditional algorithm, the proposed ray casting 3D reconstruction algorithm can reduce the time and memory cost. The experimental results show that our EDLF-CGAN has a better SR reconstruction effect than other algorithms via the indicators of the peak signal-to-noise ratio (PSNR) and structural similarity (SSIM). In addition, our advanced ray casting 3D reconstruction algorithm greatly improves the efficiency compared with the traditional ray casting algorithm.

INDEX TERMS Conditional generative adversarial network, Internet of Health Things, 3D reconstruction, super-resolution image, edge detection.

I. INTRODUCTION

The Internet of Health Things (IoHT) represents a concept that connects physical devices, networking devices,

The associate editor coordinating the review of this manuscript and approving it for publication was Muhammad Tariq¹.

intelligent devices and patient software applications [1], [2], which enable these devices to collect and transfer medical data. A patient can be remotely sensed via existing network facilities, such as tracking patients' wearable health equipment and diagnosing disease using machine learning and AI, which will send the doctors' suggestions to patients.

This approach is a new way to remotely diagnose patients at home by IoHT. When patients have medical problems or the states of a disease changes, the IoHT can reduce the time required by patients to travel to the hospital and obtain an immediate response. The IoHT would redefine healthcare systems and advance the medical communication between doctors and patients [3], [4].

When doctors remotely diagnose diseases in the IoHT, the security of CT images in the transmission process is also a very important factor [5], [6]. We assume that the proposed 3D reconstruction for super-resolution CT Images in this paper is carried out under the premise of secure data transmission in IoHT. The corresponding light weight security technique will be employed to ensure the security of CT image data. The image encryption technology is used in the transmission process of CT images, which transforms 2D CT image into one-dimensional data. In the client of the patient, the CT image is encrypted by encryption key and it can be decrypted according to the corresponding decryption key.

Besides, the accuracy of CT images seriously affects the result of diagnosis. Low-resolution medical CT images will produce low-accuracy diagnosis results for microlesions. Further, CT images cannot provide the 3D shape of an organ, which hinders doctors' diagnoses. Therefore, it is necessary to combine super-resolution technology with a 3D reconstruction algorithm to provide a more reliable basis for clinical diagnosis and surgical planning. The super-resolution technology of CT images can magnify the details of microlesions, which improves the accuracy of medical analysis. On the other hand, 3D visualization technology can display the actual morphology, which provides the overall structural information of an organ.

Deep learning has become a controversial topic and is extensively employed for 3D reconstruction of SRCT images in the IoHT. A substantial amount of related literature on this topic is available. Dong *et al.* [7] proposed the super-resolution convolutional neural networks (SRCNN) algorithm, which only applies one layer of convolution for feature extraction. There is a problem that the extracted features are local, thus the details cannot be recovered. Kim *et al.* [8] proposed an SR reconstruction algorithm based on the deeply recursive convolutional network (DRCN). Each layer of the DRCN algorithm can receive information from all previous layers. Zhang *et al.* [9] proposed a residual dense network (RDN), which adopts the residual dense block (RDB) to extract abundant local features via dense connected convolutional layers. The RDB further allows direct connections from the state of the preceding RDB to all the layers, which leads to a contiguous memory mechanism. Haris *et al.* [10] proposed deep back-projection networks (DBPN), which provide an error feedback mechanism for projection errors at each stage. However, as the depth of the network increases for these methods, the dimension of the subsequent data will be very large, which can easily cause memory error. Ledig *et al.* [11] proposed the super-resolution generative adversarial network (SRGAN), which utilizes a

discriminator network that is trained to differentiate between the super-resolved images and the original photo-realistic images. The SRGAN will not generate numerous calculations and ensures that finer texture details will be recovered.

In practice, there are many problems in the CT image processing of deep learning in the IoHT. For example, the data collection environment of a CT image will cause some inevitable problems, such as the dark tone and poor contrast of a CT image. Further, the accuracy of the edge features and unreasonable texture in a CT image have a substantial influence on the diagnosis of a disease. To solve these problems, we propose an EDLF-CGAN algorithm in the deep learning process, which adopts the conditional generative adversarial network (CGAN) [12] based on an edge detection loss function (EDLF). The CGAN is employed to generate SR images with luminance and contrast as input auxiliary conditions, which can address the unreasonable texture and improve the accuracy of SR images. An EDLF is proposed to consider the edge features in the generated SRCT images, which reduces the deformation of the generated image.

For the 3D reconstruction of CT images, the ray casting algorithm is a typical high-quality 3D reconstruction method [13]. However, the traditional ray casting algorithm has a large number of rays, which leads to a large time and memory cost. This paper proposes an advanced ray casting 3D reconstruction algorithm, which can reduce the number of rays by selecting an appropriate bounding box. We focus on the 3D reconstruction of an organ (such as the heart, liver and kidneys), which has a nearly spherical outline. Therefore, the spherical bounding box is set according to the size of the organ, and the rays that have no effect on the volume rendering results are removed. Compared with the traditional algorithm, the advanced ray casting 3D reconstruction algorithm can reduce the time and memory cost.

The contributions of this paper are listed as follows:

a) We created a 3D reconstruction method for SRCT images in the IoHT using deep learning. The evaluation shows improvement in the CT disease diagnosis scenario.

b) We created the EDLF-CGAN algorithm in the deep learning process. The CGAN adopts luminance and contrast as input auxiliary conditions to generate SRCT images, which can address the unreasonable texture and improve the accuracy. An EDLF is proposed to consider the edge features in the generated SRCT images, which reduces the deformation of the generated image.

c) We applied the SR images generated from the deep learning method to perform a 3D reconstruction. An advanced ray casting 3D reconstruction algorithm is proposed, which can reduce the number of rays by selecting an appropriate bounding box. Compared with the traditional algorithm, the advanced ray casting 3D reconstruction algorithm can reduce the time and memory cost.

The remainder of this paper is organized as follows: Section II consist of two parts. Part A presents our EDLF-CGAN algorithm in the deep learning process, and Part B shows the advanced ray casting 3D reconstruction

algorithm. In section III, we have designed and evaluated an experiment in the IoHT, which contains the performance experiment of the EDLF-CGAN algorithm and the advanced ray casting 3D reconstruction algorithm. In section IV, we have concluded our proposal with the scope of future work.

II. OUR APPROACH

A. EDLF-CGAN SUPER-RESOLUTION RECONSTRUCTION OF CT IMAGES

Due to the low-resolution medical CT images transmitted by patients in the IoHT, it is often impossible to accurately diagnose microlesions. Further, the data collection environment of the CT image will cause some inevitable problems in practice, such as the dark tone and poor contrast of the CT image [14]. To solve these problems, this paper proposes the EDLF-CGAN algorithm in the deep learning process, which adopts a conditional generative adversarial network that is based on the edge detection loss function.

1) EDLF-CGAN ALGORITHM

Our goal is to reconstruct the SR image I^{SR} from the low-resolution (LR) input image I^{LR} , and I^{SR} is as close to the HR image I^{HR} as possible. In the training process of the EDLF-CGAN, the I^{LR} corresponds to the I^{HR} for each image. This paper adopts luminance and contrast as the input auxiliary conditions, which corresponds to the HR image I_{Lum}^{HR} and $I_{Contrast}^{HR}$.

In the preparation stage of a data set, the samples of HR images are filtered by a Gaussian filter. r represents the downsampling factor of super-resolution [15], and $r = 4$ is adopted to conduct a downsampling operation to obtain the corresponding LR images. For the images with C channels [16], I^{LR} is represented by a tensor of size $W \times H \times C$, and I^{HR} and I^{SR} are described by $rW \times rH \times C$.

The EDLF-CGAN consists of generator (G) and discriminator (D) networks, and its goal is to obtain the generator network G via training. By the input auxiliary conditions and I^{LR} , the generator network G can obtain the corresponding I^{HR} . Our goal is to make the generated HR image more similar to the original HR image. A feed-forward convolution neural network is trained [17], and its parameter set is $\theta_{G|y}$, where $\theta_{G|y} = \{W_{1:L}; b_{1:L}\}$ represents the weights $W_{1:L}$ and biases $b_{1:L}$ of the L-layer network. The LR training images are represented by $I_{n|y}^{LR}$ ($n = 1, \dots, N$), and the corresponding HR images are described as $I_{n|y}^{HR}$ ($n = 1, \dots, N$), where the subscript indicates the input auxiliary condition y and N is the size of the training data set. I^{SR} is the loss function [18] of the EDLF-CGAN. The core objectives of the EDLF-CGAN can be expressed by formula (1):

$$\hat{\theta}_{G|y} = \arg \min_{\theta_{G|y}} \frac{1}{N} \sum_{n=1}^N I^{SR} \left(G_{\theta_{G|y}} \left(I_{n|y}^{LR} \right), I_{n|y}^{HR} \right) \quad (1)$$

where $\hat{\theta}_{G|y}$ represent the parameters of the generator network. According to formula (1), the goal of the EDLF-CGAN is

to produce the parameters $\hat{\theta}_{G|y}$ of the generator network. Therefore, we obtain the SR image $G_{G|y} \left(I_{n|y}^{LR} \right)$, which is closest to the HR image $I_{n|y}^{HR}$ and satisfies the input auxiliary condition y .

2) NETWORK ARCHITECTURE

We adopt the U-Net architecture to perform concatenation of the higher level and lower level feature maps by the skip connection so that the pixel detail information at different resolutions is retained. The generator of the EDLF-CGAN adopts the symmetrical convolutional neural network structure, and the discriminator refers to the VGG network [19].

① GENERATOR

The front part of the generator is employed for feature extraction and nonlinear mapping of LR images. The latter part is to reconstruct the corresponding HR images from the extracted features. The generator adopts the fast up-convolutions [20] to realize the $4 \times$ upsampling, which can greatly reduce the checkerboard effect of the network. The generator magnifies an image twice by upsampling, and each time it magnifies $2 \times$. The convolution layer of the generator is followed by the batch normalization layer and the activation function layer of the parametric ReLU [21]. Figure 1 shows the generator structure of the EDLF-CGAN.

In Figure 1, the convolutional layer is represented by a blue box, and the number of feature maps, strides and kernels is shown at the top of the blue boxes. The stride convolutional layer is applied for the downsampling operation and represented by a purple box. The number of feature maps, strides and kernels is shown at the bottom of the purple boxes. The fast up-convolution is represented by an orange box, and the number of feature maps, strides and kernels are shown at the bottom of the orange boxes. The batch-normalization layer is indicated by a yellow box, and the activation function of the ReLU is represented by a green box.

Fast up-convolution adjusts the up-sampling operation to make it more efficient. The convolution kernel with the original size of 5×5 is reset to four small sizes: (a) 3×3 , (b) 3×2 , (c) 2×3 , and (d) 2×2 . By interleaving four feature maps, the image can be magnified $2 \times$. This operation can greatly reduce the checkerboard effect caused by traditional de-convolution and upsampling.

② DISCRIMINATOR

The discriminator structure of the EDLF-CGAN is shown in Figure 2. The convolutional layer is represented by a blue box, and the number of feature maps, strides and kernels are shown at the top of the blue boxes. The batch normalization is indicated by a gray box. The activation function of the Leaky ReLU is a nonlinear activation function with the slope parameter $\alpha = 0.2$, which is represented by a pink box. The global average pooling [22] is represented by a purple box. The sigmoid function [23] is shown at the last layer of the network and represented by an orange box.

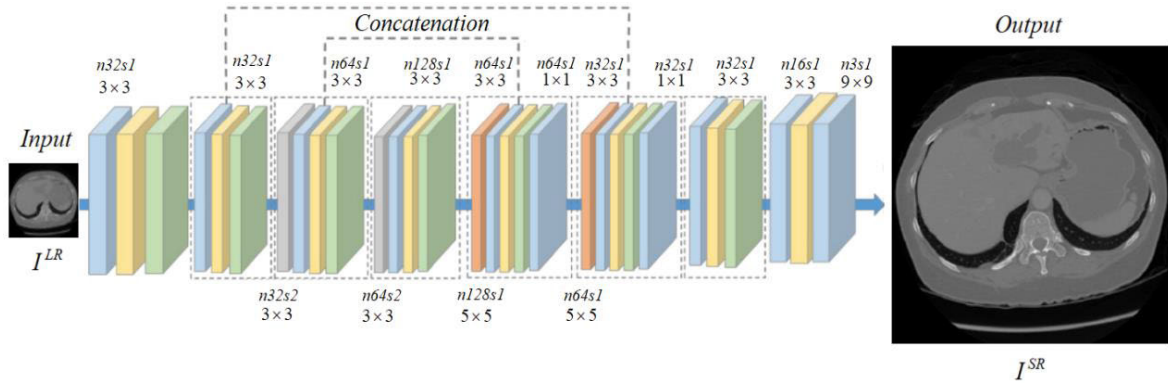


FIGURE 1. Generator structure of EDLF-CGAN with corresponding number of feature maps (n), strides (s) and kernels.

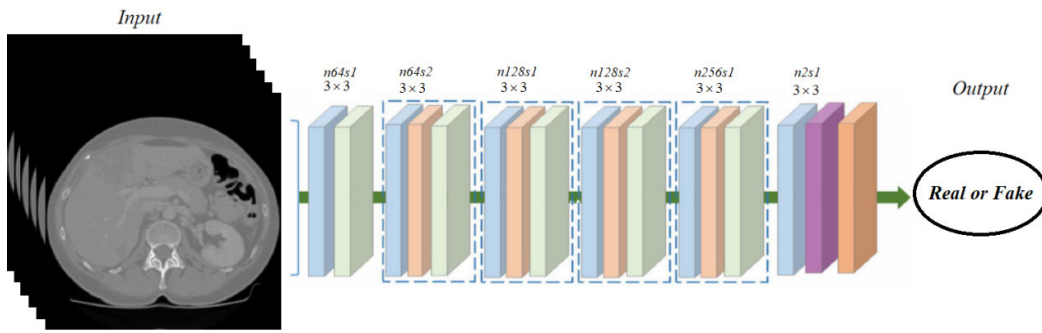


FIGURE 2. Discriminator structure of EDLF-CGAN with corresponding number of feature maps (n), strides (s) and kernels.

3) OBJECTIVE FUNCTION

The objective function in our paper consists of two parts: the edge detection loss function (EDLF) l_{Edge}^{SR} and the perceptual loss function $l_{Perceptual}^{SR}$. Edge detection usually extracts the drastic changes in the pixels in the image as the edge. Adding the EDLF l_{Edge}^{SR} to the training process of the generator will reduce the deformation of the generated image. The perceptual loss function $l_{Perceptual}^{SR}$ is the weighted sum of the content loss function l_{MSE}^{SR} [24] and the adversarial loss function l_{Gen}^{SR} [25]. The content loss function l_{MSE}^{SR} is a loss function that uses the root mean square error (MSE), which can improve the PSNRs of SR images, but it would blur the details of images. The requirement of the adversarial loss function l_{Gen}^{SR} is to maximize the probability estimation of the generated image and the real sample, which is helpful for recovering the realistic details of an image.

① EDLF

We have researched and compared many edge detection operators and discovered that the Canny operator [26] would obtain clear details and texture. The main idea of edge detection is to use a filter to reduce the noise of an image, calculate the gradient value and direction in an image, and apply the double threshold strategy to connect the edge. The EDLF is

defined as shown in formula (2):

$$l_{Edge}^{SR} = \frac{1}{r^2WH} \sum_{x=1}^{rW} \sum_{y=1}^{rH} \left(C(I_y^{HR})_{x,y} - C(I_y^{SR})_{x,y} \right)^2 \quad (2)$$

where W and H represent the width and height, respectively, of the LR image. r is the downsampling factor of super-resolution. I_y^{HR} represent the original HR images that satisfy the condition y . $(I_y^{HR})_{x,y}$ represents the pixel value at the location (x, y) in the HR image. I_y^{SR} represents the SR image generated by G , which satisfies the condition y . C represents the Canny edge detection function. The expected results of training is to reduce the value of l_{Edge}^{SR} , which can suppress the generation of unreasonable texture information.

② PERCEPTUAL LOSS FUNCTION

The perceptual loss function $l_{Perceptual}^{SR}$ is shown in formula (3):

$$l_{Perceptual}^{SR} = l_{MSE}^{SR} + \beta l_{Gen}^{SR} \quad (3)$$

where the value of β is 10^{-3} . The MSE loss function is shown in formula (4):

$$l_{MSE}^{SR} = \frac{1}{r^2WH} \sum_{x=1}^{rW} \sum_{y=1}^{rH} \left((I_y^{HR})_{x,y} - (I_y^{SR})_{x,y} \right)^2 \quad (4)$$

where W and H represent the width and the height, respectively, of the LR image.

The adversarial loss function l_{Gen}^{SR} tends to deceive the discriminator D and focuses on the generation of high-quality images. The definition of l_{Gen}^{SR} is shown in formula (5):

$$l_{Gen}^{SR} = \sum_{n=1}^N \left[-\log D_{\theta_{Dly}} \left(I_y^{SR} \right) \right] \quad (5)$$

where N represents the size of the training data. $D_{\theta_{Dly}} \left(I_y^{SR} \right)$ is the probability that the discriminator $D_{\theta_{Dly}}$ judges I_y^{SR} as false.

B. ADVANCED RAY CASTING 3D RECONSTRUCTION ALGORITHM

We apply the SR images generated from the deep learning method to perform a 3D reconstruction in the IoHT. The ray casting algorithm is a typical high-quality 3D reconstruction method. However, the traditional ray casting algorithm has a large number of rays, which leads to a large time and memory cost [27].

This paper proposes an advanced ray casting 3D reconstruction algorithm, which can reduce the number of rays by selecting an appropriate bounding box. We focus on the 3D reconstruction of an organ (such as the heart, liver and kidneys), which has a nearly spherical outline. Therefore, the spherical bounding box is set according to the size of the organ, and the rays that have no effect on the volume rendering result are removed.

1) SETTING OF SPHERICAL BOUNDING BOX

Selecting an appropriate bounding box can reduce the number of rays during rendering [28]. The bounding box should be as small as possible and should accommodate the 3D data field. This paper adopts a spherical bounding box to reduce the number of rays. The measurement of the regular 3D data field is represented by *length*, *width* and *height*. The radius of the spherical bounding box is set as:

$$Radius = \frac{1}{2} \times \text{Max} (\text{length}, \text{width}, \text{height}) \quad (6)$$

The advantages of the spherical bounding box are listed as follows: ① the number of rays is greatly reduced; ② when the viewpoint position changes, the resampling points do not need to be recalculated.

2) DATA FIELD REDUCTION ALGORITHM

Calculate the intersection number of the ray and spherical bounding boxes, and remove the ray that has no effect on the volume rendering results. The data field reduction algorithm consists of three steps:

Step 1: Define the equation of the spherical bounding box. The central coordinates of the 3D data field are $(0, 0, z')$. The equation of the spherical bounding box can be described as follows:

$$x^2 + y^2 + (z - z')^2 = \text{Radius}^2 \quad (7)$$

Step 2: Define the equation for the ray, which can be expressed by formula (8):

$$\begin{cases} x = x_0 + lt \\ y = y_0 + mt \\ z = z_0 + nt \end{cases} \quad (8)$$

where (l, m, n) represents the direction vector of the ray, and (x_0, y_0, z_0) represents one point on it.

Step 3: Calculate the intersection number of the ray and spherical bounding box. Combine formula (7) and formula (8) to obtain formula (9):

$$(x_0 + lt)^2 + (y_0 + mt)^2 + (z_0 + nt - z')^2 = \text{Radius}^2 \quad (9)$$

If the solution of formula (9) has two intersections, then the ray intersects the spherical bounding box. After the judgment of formula (9), remove the rays that do not intersect the spherical bounding box, and ensure that each ray intersects the volume data.

III. EXPERIMENTS

The IoHT represents a set of medical devices and applications that are connected to healthcare systems via online networks. The 3D reconstruction algorithm for SRCT images in the IoHT using deep learning can remotely diagnose the disease, which directly integrates all medical resources to serve patients. For performance evaluation of deep learning, we select 2000 CT images of the liver from the 3D-IRCADb-01 database [29] (<https://www.ircad.fr/research/3d-ircadb-01/>). The 3D-IRCADb-01 database is composed of the 3D CT scans of 10 women and 10 men with liver tumors in 75% of cases. Twenty folders correspond to 20 different patients, which contain approximately 100 images for each anonymized patient in DICOM format.

To evaluate the effect of the 3D reconstruction method for SRCT images in the IoHT using deep learning, we simulate the method by the computers in the IoHT. First, the original high-resolution (HR) images obtain the corresponding LR images by downsampling. The simulated LR images are generated on ThinkPad S3-490, of which the processor is Intel(R) Core(TM)i5-8265U CPU@1.60 GHz with 8 GB of memory. The algorithm of the simulated LR images is realized by MATLAB 2018b. Second, the EDLF-CGAN algorithm runs on a computer that is equipped with GeForce RTX 2080Ti GPU and realized by Python. Moreover, the advanced ray casting 3D reconstruction algorithm runs in ThinkPad S3-490 for a liver CT image, which is realized by visual studio 2019.

A. EXPERIMENT OF EDLF-CGAN SUPER-RESOLUTION RECONSTRUCTION

Consider the diagnosis results of two liver tumor patients as examples. Figure 3 shows two CT images of a male liver patient who has one tumor in zone IV. Figure 4 shows two CT images of a female liver patient who has one tumor in zone III.

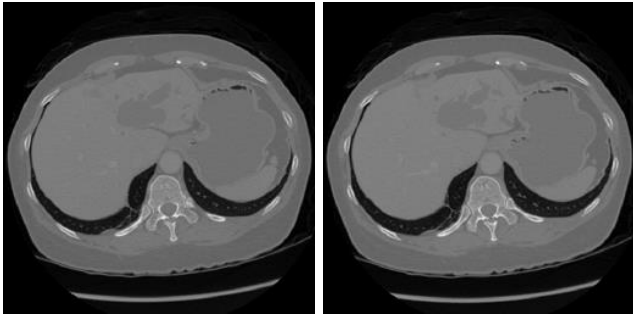


FIGURE 3. CT images of male liver patient who has one tumor in zone IV.

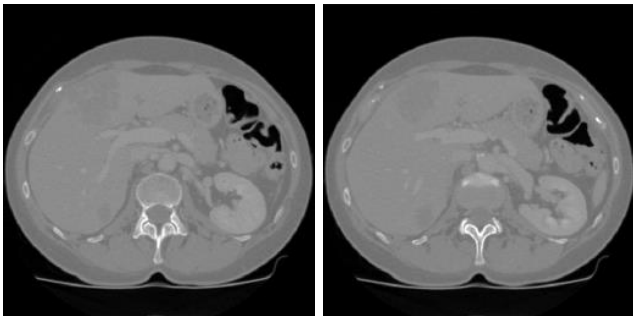


FIGURE 4. CT images of female liver patient who has one tumor in zone III.

1) GENERATION OF LOW-RESOLUTION IMAGES

Because MATLAB has a library function for resizing the image, namely imresize function, we apply the imresize function to perform a downsampling operation for HR images (downsampling factor is $r = 4$). The size of the original HR CT image is 512×512 pixels, and the size of the corresponding LR CT image is 128×128 pixels. Crop the LR image into blocks of 64×64 pixels without overlapping, and crop HR CT images into blocks of 256×256 pixels. The image blocks that correspond to high and low resolution are employed for training.

In Figure 5, (a) shows the original HR CT images of a male liver patient who has one tumor in zone IV and (b) shows the corresponding LR CT images. In Figure 6, (a) shows the original HR CT images of a female liver patient who has one tumor in zone III and (b) shows the corresponding LR CT images.

2) PERFORMANCE OF EDLF-CGAN

① QUALITATIVE EVALUATION

We trained EDLF-CGAN on CT images conditioned on their luminance and contrast labels. For different classic SR algorithms, our algorithm is compared with the Bicubic algorithm [30], SRCNN algorithm [7], DRCN algorithm [8] and SRGAN algorithm [11]. Figure 7 shows the SR images of various algorithms for a male liver patient who has one tumor in zone IV, and Figure 8 shows the SR images of various algorithms for a female liver patient who has one tumor in zone III.

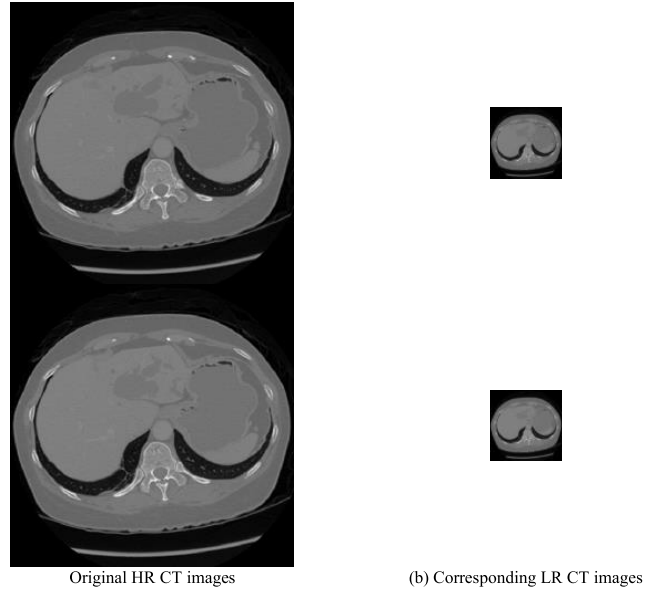


FIGURE 5. Results of different resolutions of male liver tumor patient in zone IV.

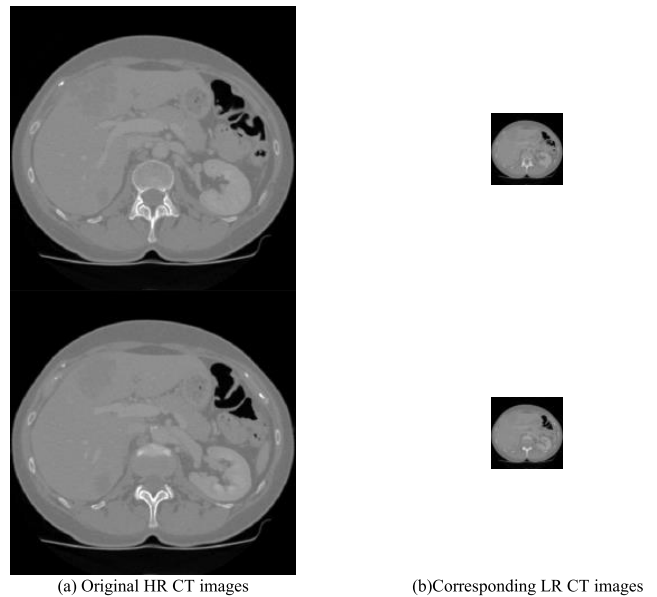


FIGURE 6. Results of different resolution of female liver patient who has one tumor in zone III.

In Figure 7 and Figure 8, (a) represents the original HR image, (b) represents the corresponding LR image, (c) represents the SR image of the Bicubic algorithm, (d) represents the SR image of the SRCNN algorithm, (e) represents the SR image of the DRCN algorithm, (f) represents the SR image of the SRGAN algorithm, (g) represents the SR image of the EDLF-CGAN algorithm with the luminance input condition, and (h) represents the SR image of the EDLF-CGAN with the contrast input condition.

The results in Figure 7 and Figure 8 show that the Bicubic algorithm can be easily realized but the details of the reconstructed image are obviously fuzzy. The experimental

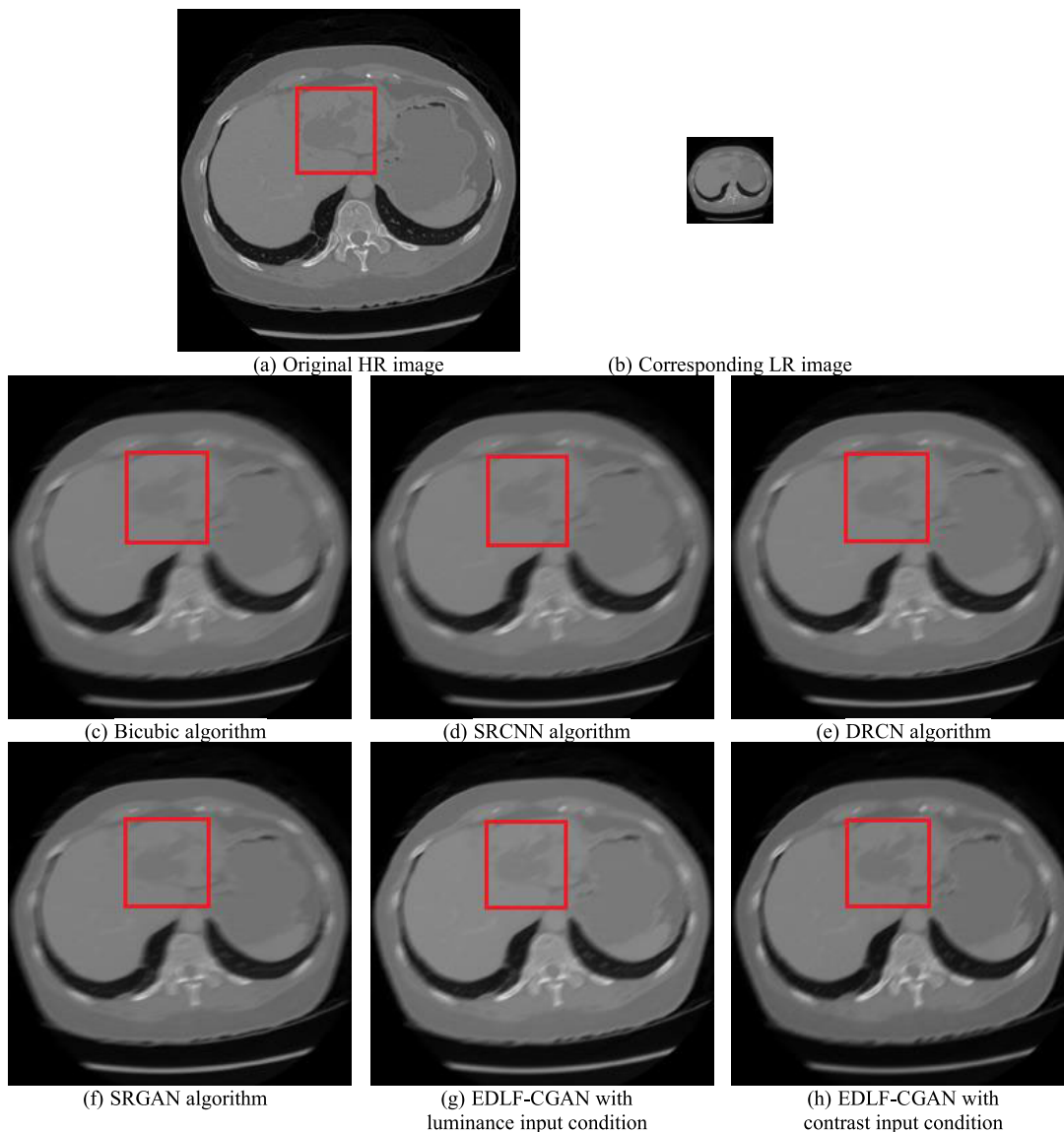


FIGURE 7. SR images of various algorithms of male liver tumor patient in zone IV.

results of the SRCNN algorithm show that the edge is slightly visible with a gap compared with the original HR image. The DRCN can obtain better reconstruction results than SRCNN but the mean square error is considered as the optimization goal, which causes the reconstructed image to lack perceptual information. Compared with the former three algorithms, SRGAN can reconstruct more high-frequency details of the image, and the edge is clearer. Our EDLF-CGAN adopts luminance and contrast as input conditions, and the SR reconstruction results of the generator are more suitable for CT images.

We further investigated the effect of different loss functions. Figure 9 and Figure 10 show the SR images of different loss functions for two liver tumor patients.

$CGAN + l_{Perceptual}^{SR}$: CGAN applies the perceptual loss function $l_{Perceptual}^{SR}$.

$CGAN + l_{Perceptual}^{SR} + l_{Edge}^{SR}$: CGAN employs the perceptual loss function $l_{Perceptual}^{SR}$ and EDLF l_{Edge}^{SR} .

The results of Figure 9 and Figure 10 show that the reconstruction details of the $CGAN + l_{Perceptual}^{SR}$ and SR images are fuzzy. $CGAN + l_{Perceptual}^{SR} + l_{Edge}^{SR}$ is more helpful for restoring the realistic edge texture and high-frequency details of the reconstructed image.

② QUANTITATIVE EVALUATION

We evaluated the effect of CT image restoration using the following two evaluation indicators: peak signal-to-noise ratio (PSNR) [31] and structural similarity (SSIM) [32].

The PSNR is a statistical analysis indicator that is based on the gray value of image pixels, which is defined by the mean square error (MSE) between the original image $I(i, j)$ and the

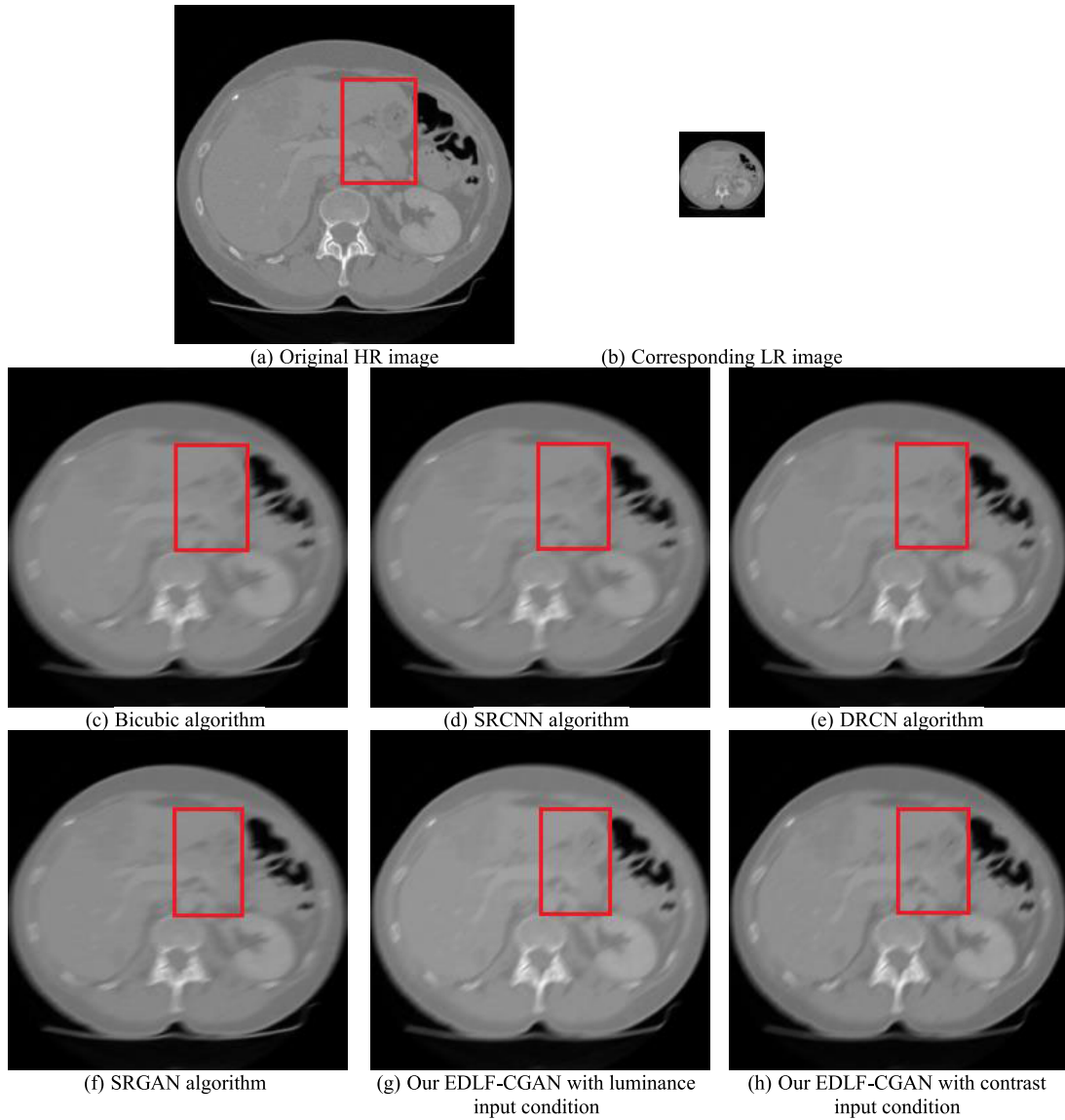


FIGURE 8. SR images of various algorithms of female liver tumor patient in zone III.

restored image $K(i, j)$. Generally, the higher the PSNR value is, the better the image restoration is

$$PSNR = 10 \times \log_{10} \left(\frac{(2^n - 1)^2}{MSE} \right) \quad (10)$$

$$MSE = \frac{1}{mn} \sum_{i=0}^m \sum_{j=0}^n \|I(i, j) - K(i, j)\|^2 \quad (11)$$

SSIM is a similarity indicator of two images. The first image is the original HR image, and the second image is the SR reconstructed image.

For the two images x and y , the structural similarity of the two images is defined as

$$SSIM(x, y) = l(x, y)^\alpha \cdot c(x, y)^\beta \cdot s(x, y)^\gamma \quad (12)$$

where $l(x, y)$, $c(x, y)$, $s(x, y)$ represent the luminance, contrast and structure of the image, and α , β , and γ are greater than 0.

$$l(x, y) = \frac{2\mu_x\mu_y + C_1}{\mu_x^2 + \mu_y^2 + C_1} \quad (13)$$

$$c(x, y) = \frac{2\delta_x\delta_y + C_2}{\delta_x^2 + \delta_y^2 + C_2} \quad (14)$$

$$s(x, y) = \frac{\delta_{xy} + C_3}{\delta_x\delta_y + C_3} \quad (15)$$

where μ_x and μ_y represent all pixels in the image x and y ; δ_x and δ_y are the standard deviations of the image pixel; and δ_{xy} is the covariance of images x and y . C_1 , C_2 , and C_3 are constants that are employed to avoid the error when the denominator of formulas (13)~(15) is 0.

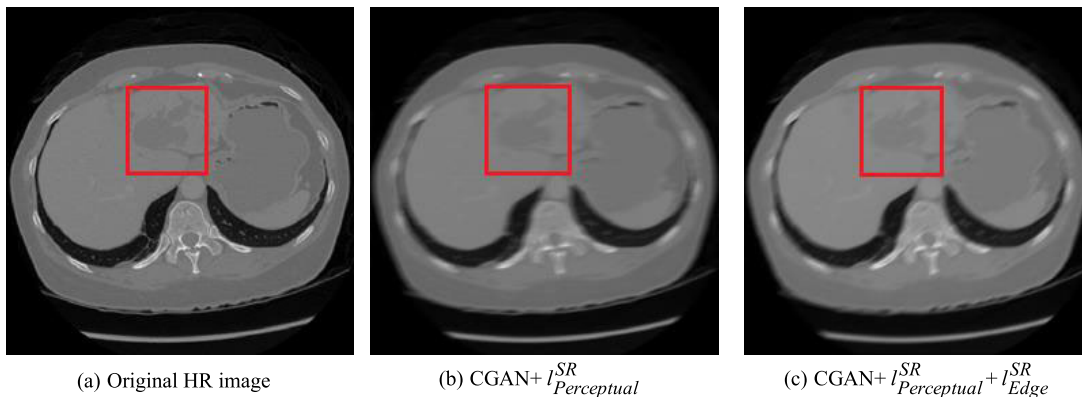


FIGURE 9. SR images of different loss functions of male liver tumor patient in zone IV.

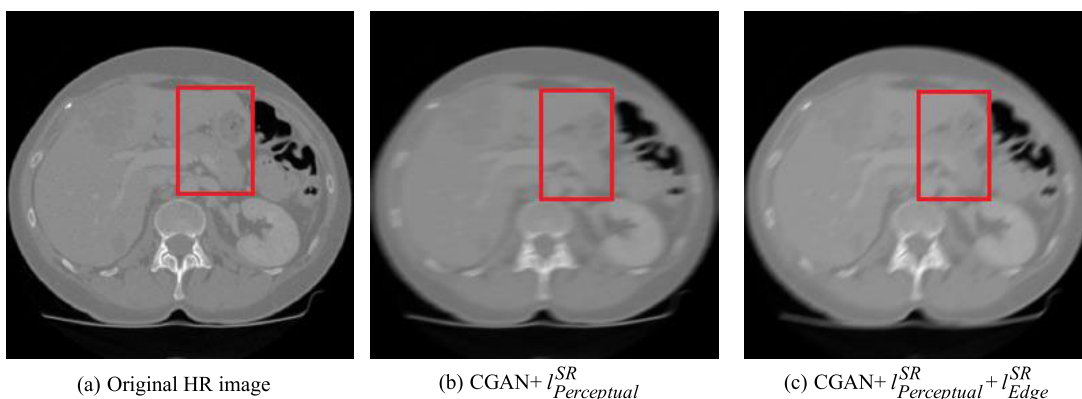


FIGURE 10. SR images of various algorithms of female liver tumor patient in zone III.

In the application, the set $\alpha = \beta = \gamma = 1$, $C_3 = 0.5C_2$, and SSIM is expressed as follows:

$$SSIM(x, y) = \frac{(2\mu_x\mu_y + C_1)(2\delta_{xy} + C_2)}{(\mu_x^2 + \mu_y^2 + C_1)(\delta_x^2 + \delta_y^2 + C_2)} \quad (16)$$

The range of structural similarity is 0 to 1. When the two images are the same, the value of SSIM is equal to 1.

For the SR images of the two liver tumor patients, the values of PSNR and SSIM of the Bicubic algorithm, SRCNN algorithm, DRCN algorithm, SRGAN algorithm, EDLF-CGAN algorithm with luminance input condition, and EDLF-CGAN algorithm with contrast input condition are shown in Table 1 and Table 2. It can be seen that the PSNR value of our EDLF-CGAN algorithm is greater than the other four representative algorithms. The SSIM value of our EDLF-CGAN algorithm is close to 1, which achieves a better reconstruction effect.

For the SR images of two liver tumor patients, the results of PSNR and SSIM of different loss functions are shown in Table 3 and Table 4. After combining the edge detection loss l_{Edge}^{SR} with the perceptual loss $l_{Perceptual}^{SR}$, a higher PSNR value is obtained. The SR reconstruction image of the perceptual loss function $l_{Perceptual}^{SR}$ is smoother and less convincing,

which is caused by competition between the MSE-based content loss l_{MSE}^{SR} and the adversarial loss l_{Gen}^{SR} .

B. 3D RECONSTRUCTION EXPERIMENT

By CT images of two liver tumor patients, 3D reconstruction is performed. A total of 200 CT images of a male liver patient who has one tumor in zone IV are selected. A total of 129 CT images are selected of a female liver patient who has one tumor in zone III. The size of the CT image is 512×512 pixels. Therefore, the dimensions of the two data sets are $512 \times 512 \times 200$ and $512 \times 512 \times 129$.

1) PERFORMANCE OF 3D RECONSTRUCTION

In the performance of the 3D reconstruction comparative experiment, the traditional ray casting algorithm and our algorithm are employed to reconstruct the CT images of two liver tumor patients.

Table 5 shows the comparison results of 3D reconstruction. For two liver tumor patients, our algorithm greatly reduces the time and memory cost of 3D reconstruction. The traditional ray casting algorithm has a large number of rays, which produces a very large time and memory cost. Our algorithm adopts the spherical bounding box to reduce the

TABLE 1. PSNR and SSIM of different algorithms of male liver tumor patient in zone IV.

Similarity Indicator	Comparison Algorithm					
	Bicubic algorithm	SRCNN algorithm	DRCN algorithm	SRGAN algorithm	EDLF-CGAN with luminance input condition	EDLF-CGAN with contrast input condition
PSNR	31.9073	32.4129	33.2866	34.0333	34.5104	34.3831
SSIM	0.8287	0.8426	0.8644	0.8826	0.8963	0.8930

TABLE 2. PSNR and SSIM of different algorithms of female liver tumor patient in zone III.

Similarity Indicator	Comparison Algorithm					
	Bicubic algorithm	SRCNN algorithm	DRCN algorithm	SRGAN algorithm	EDLF-CGAN with luminance input condition	EDLF-CGAN with contrast input condition
PSNR	32.6978	33.2478	33.8218	34.2231	34.7458	34.6462
SSIM	0.8441	0.8583	0.8731	0.8835	0.8970	0.8944

TABLE 3. PSNR and SSIM of different loss functions of male liver tumor patient in zone IV.

Similarity Indicator	Comparison Algorithm	
	CGAN+ $l_{Perceptual}^{SR}$	CGAN+ $l_{Perceptual}^{SR}$ + l_{Edge}^{SR}
PSNR	34.2256	34.5104
SSIM	0.8856	0.8963

TABLE 4. PSNR and SSIM of different loss functions of female liver tumor patient in zone III.

Similarity Indicator	Comparison Algorithm	
	CGAN+ $l_{Perceptual}^{SR}$	CGAN+ $l_{Perceptual}^{SR}$ + l_{Edge}^{SR}
PSNR	34.3225	34.7458
SSIM	0.8862	0.8970

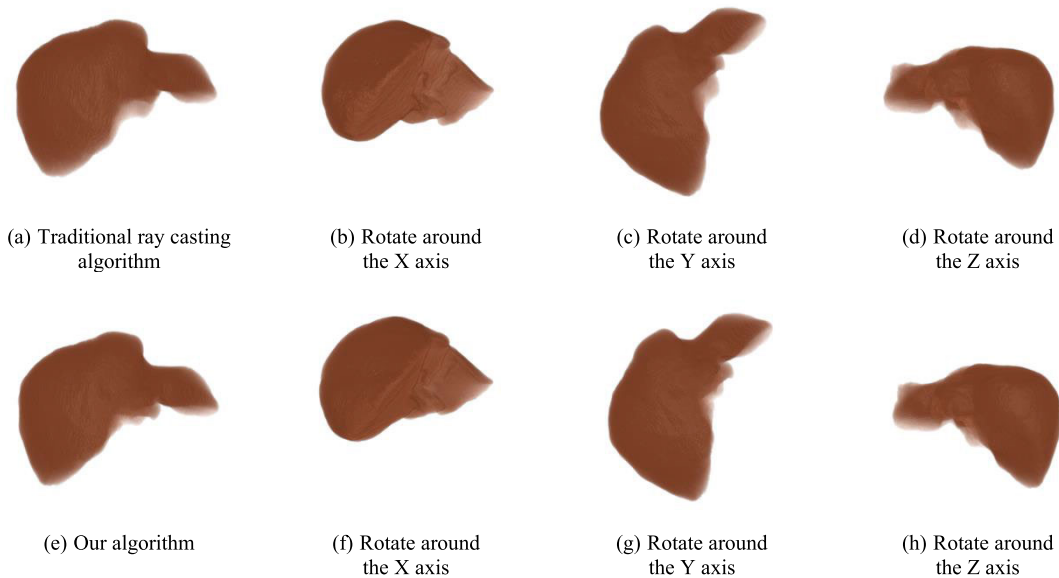


FIGURE 11. 3D reconstruction results of the male liver tumor patient in zone IV.

number of rays, which greatly improves the efficiency of 3D reconstruction.

2) RESULTS OF 3D RECONSTRUCTION

To compare the accuracy of the traditional ray casting algorithm with our algorithm, Figure 11 and Figure 12 show the

3D reconstruction results of these two algorithms rotating around the X, Y and Z axes, where (a)~(d) are the 3D reconstruction results of the traditional ray casting algorithm and (e)~(h) are the 3D reconstruction results of our algorithm. Figure 11 shows the 3D reconstruction results of the male liver patient who has one tumor in zone IV. Figure 12 shows

TABLE 5. Comparison results of 3D reconstruction.

Data Set	Data Dimension	Algorithm Name	Memory Cost (K Byte)	Time Cost (ms)
Male liver tumor patient in zone IV	512 × 512 × 200	Traditional ray casting algorithm	89381	12817
		Our algorithm	87525	585
Female liver tumor patient in zone III	512 × 512 × 129	Traditional ray casting algorithm	49554	7966
		Our algorithm	48242	241

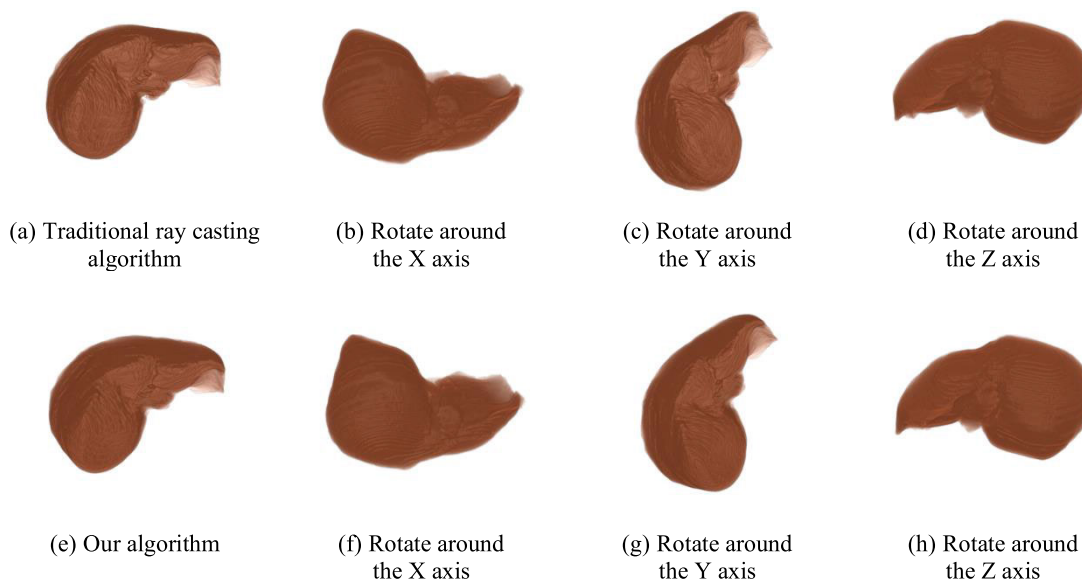


FIGURE 12. 3D reconstruction results of the female liver patient who has one tumor in zone III.

the 3D reconstruction results of the female liver patient who has one tumor in ZONE III. Compared with the traditional algorithm, our advanced ray casting 3D reconstruction algorithm also presents a reasonable reconstruction effect.

IV. CONCLUSION

In this paper, a 3D reconstruction method for SRCT images in the IoHT using deep learning is proposed. First, we adopt deep learning to obtain SRCT images from low-resolution images in the IoHT. We propose an EDLF-CGAN algorithm in the deep learning process, the CGAN is employed to generate SRCT images with luminance and contrast as the input auxiliary conditions, which can improve the accuracy of SR images. An EDLF is proposed to consider the edge features in the generated SRCT images, which reduces the deformation of generated image. Second, we employ the SR images generated from the deep learning method to perform 3D reconstruction. An advanced ray casting 3D reconstruction algorithm is proposed, which can reduce the number of rays by selecting an appropriate bounding box. Compared with the traditional algorithm, the advanced ray casting 3D

reconstruction algorithm can reduce the time and memory cost.

With the high-accuracy and high-security 3D reconstruction results [33], the IoHT can remotely diagnose diseases, which directly integrates all medical resources to serve patients. On the one hand, the IoHT application of diagnosing disease via machine learning and AI is valuable for the patients to get the high-accuracy diagnosis result. On the other hand, lightweight security provides patients with the security of CT image data transmission and the confidentiality of local storage. In the future, the IoHT will exist in our life in various forms, such as tracking patients' wearable health equipment, monitoring the growth of children, preventing the diseases of middle-aged people, and controlling the status of the elderly. The IoHT would provide convenient medical treatment and contribute to improving the health of humans [34].

ACKNOWLEDGMENT

(Jing Zhang, Ling-Rui Gong, Keping Yu, and Xin Qi are co-first authors.)

REFERENCES

- [1] A. C. Cristiano, C. F. Pasluosta, B. Eskofier, B. S. Denise, and R. R. Rodrigo, "Internet of health things: Toward intelligent vital signs monitoring in hospital wards," *Artif. Intell. Med.*, vol. 89, no. 6, pp. 61–69, 2018, doi: [10.1016/j.artmed.2018.05.005](https://doi.org/10.1016/j.artmed.2018.05.005).
- [2] X. Zhou, W. Liang, K. I.-K. Wang, H. Wang, L. T. Yang, and Q. Jin, "Deep learning enhanced human activity recognition for Internet of healthcare things," *IEEE Internet Things J.*, early access, Apr. 2, 2020, doi: [10.1109/JIOT.2020.2985082](https://doi.org/10.1109/JIOT.2020.2985082).
- [3] J. J. P. C. Rodrigues, D. B. De Rezende Segundo, H. A. Junqueira, M. H. Sabino, R. M. Prince, J. Al-Muhtadi, and V. H. C. De Albuquerque, "Enabling technologies for the Internet of health things," *IEEE Access*, vol. 6, pp. 13129–13141, 2018, doi: [10.1109/ACCESS.2017.2789329](https://doi.org/10.1109/ACCESS.2017.2789329).
- [4] X. Zhou, Y. Li, and W. Liang, "CNN-RNN based intelligent recommendation for online medical pre-diagnosis support," *IEEE/ACM Trans. Comput. Biol. Bioinf.*, early access, May 14, 2020, doi: [10.1109/TCBB.2020.2994780](https://doi.org/10.1109/TCBB.2020.2994780).
- [5] M. Kamal and M. Tariq, "Light-weight security and data provenance for multi-hop Internet of Things," *IEEE Access*, vol. 6, pp. 34439–34448, 2018, doi: [10.1109/ACCESS.2018.2850821](https://doi.org/10.1109/ACCESS.2018.2850821).
- [6] M. Kamal and M. Tariq, "Light-weight security and blockchain based provenance for advanced metering infrastructure," *IEEE Access*, vol. 7, pp. 87345–87356, 2019, doi: [10.1109/ACCESS.2019.2925787](https://doi.org/10.1109/ACCESS.2019.2925787).
- [7] C. Dong, C. C. Loy, K. He, and X. Tang, "Image super-resolution using deep convolutional networks," *IEEE Trans. Pattern Anal. Mach. Intell.*, vol. 38, no. 2, pp. 295–307, Feb. 2016, doi: [10.1109/TPAMI.2015.2439281](https://doi.org/10.1109/TPAMI.2015.2439281).
- [8] J. Kim, J. K. Lee, and K. M. Lee, "Deeply-recursive convolutional network for image super-resolution," in *Proc. IEEE Conf. Comput. Vis. Pattern Recognit. (CVPR)*. Las Vegas, NV, USA: IEEE, Jun. 2016, p. 2016.
- [9] Y. Zhang, Y. Tian, Y. Kong, B. Zhong, and Y. Fu, "Residual dense network for image super-resolution," in *Proc. IEEE/CVF Conf. Comput. Vis. Pattern Recognit.* Salt Lake City, UT, USA: IEEE, Jun. 2018, pp. 2472–2481.
- [10] M. Haris, G. Shakhnarovich, and N. Ukita, "Deep back-projection networks for super-resolution," in *Proc. IEEE/CVF Conf. Comput. Vis. Pattern Recognit.* Salt Lake City, UT, USA: IEEE, Jun. 2018, pp. 1664–1673.
- [11] C. Ledig, L. Theis, F. Huszar, J. Caballero, A. Cunningham, A. Acosta, A. Aitken, A. Tejani, J. Totz, Z. Wang, and W. Shi, "Photo-realistic single image super-resolution using a generative adversarial network," in *Proc. IEEE Conf. Comput. Vis. Pattern Recognit. (CVPR)*. Honolulu, HI, USA: IEEE, Jul. 2017, pp. 105–114.
- [12] R. Li, J. Pan, Z. Li, and J. Tang, "Single image dehazing via conditional generative adversarial network," in *Proc. IEEE/CVF Conf. Comput. Vis. Pattern Recognit.* Salt Lake City, UT, USA: IEEE, Jun. 2018, pp. 655–669.
- [13] J. Tan, J. Chen, Y. Wang, L. Li, and Y. Bao, "Design of 3D visualization system based on VTK utilizing marching cubes and ray casting algorithm," in *Proc. 8th Int. Conf. Intell. Hum.-Mach. Syst. Cybern. (IHMSC)*. Hangzhou, China: IEEE, Aug. 2016, pp. 192–197.
- [14] H. Sui, L. Liu, X. Li, P. Zuo, J. Cui, and Z. Mo, "CT-based radiomics features analysis for predicting the risk of anterior mediastinal lesions," *J. Thoracic Disease*, vol. 11, no. 5, pp. 1809–1818, May 2019, doi: [10.21037/jtd.2019.05.32](https://doi.org/10.21037/jtd.2019.05.32).
- [15] M. Shen, P. Xue, and C. Wang, "Down-sampling based video coding using super-resolution technique," *IEEE Trans. Circuits Syst. Video Technol.*, vol. 21, no. 6, pp. 755–765, Jun. 2011, doi: [10.1109/TCSVT.2011.2130390](https://doi.org/10.1109/TCSVT.2011.2130390).
- [16] H.-C. Huang and F.-C. Chang, "Visual cryptography for compressed sensing of images with transmission over multiple channels," in *Proc. Int. Conf. Intell. Inf. Hiding Multimedia Signal Process. (IHH-MSP)*. Adelaide, SA, Australia: IEEE, Sep. 2015, pp. 21–24.
- [17] J. Zou, Q. Wu, Y. Tan, F. Wu, and W. Wang, "Analysis range of coefficients in learning rate methods of convolution neural network," in *Proc. 14th Int. Symp. Distrib. Comput. Appl. Bus. Eng. Sci. (DCABES)*. Guiyang, China: IEEE, Aug. 2015, pp. 513–517.
- [18] Y.-Y. Shi, X.-J. Wang, and Q. Zhang, "The constrained optimization extreme learning machine based on the hybrid loss function for regression," in *Proc. 10th Int. Conf. Adv. Comput. Intell. (ICACI)*. Xiamen, China: IEEE, Mar. 2018, pp. 336–342.
- [19] I. Ha, H. Kim, S. Park, and H. Kim, "Image retrieval using BIM and features from pretrained VGG network for indoor localization," *Building Environ.*, vol. 140, pp. 23–31, Aug. 2018, doi: [10.1016/j.buildenv.2018.05.026](https://doi.org/10.1016/j.buildenv.2018.05.026).
- [20] I. Laina, C. Rupprecht, V. Belagiannis, F. Tombari, and N. Navab, "Deeper depth prediction with fully convolutional residual networks," in *Proc. 4th Int. Conf. 3D Vis. (3DV)*, Oct. 2016, pp. 1–12.
- [21] A. Gupta and R. Duggal, "P-TELU: Parametric tan hyperbolic linear unit activation for deep neural networks," in *Proc. IEEE Int. Conf. Comput. Vis. Workshops (ICCVW)*, Oct. 2017, pp. 974–978.
- [22] B. Zhou, A. Khosla, A. Lapedriza, A. Oliva, and A. Torralba, "Learning deep features for discriminative localization," in *Proc. IEEE Conf. Comput. Vis. Pattern Recognit. (CVPR)*. Las Vegas, NV, USA: IEEE, Jun. 2016, pp. 2921–2929.
- [23] P. Milanov, G. Koroleova, R. Mavrevski, and N. Pencheva, "Curve fitting problem: Torque–velocity relationship with polynomials and Boltzmann sigmoid functions," *Acta Bioeng. Biomech.*, vol. 20, no. 1, pp. 169–184, 2018, doi: [10.5277/ABB-01048-2017-03](https://doi.org/10.5277/ABB-01048-2017-03).
- [24] L. Chen, H. Qu, J. Zhao, B. Chen, and J. C. Principe, "Efficient and robust deep learning with correntropy-induced loss function," *Neural Comput. Appl.*, vol. 27, no. 4, pp. 1019–1031, May 2016, doi: [10.1007/s00521-015-1916-x](https://doi.org/10.1007/s00521-015-1916-x).
- [25] G. Kim, H. Lee, B.-K. Kim, S.-H. Oh, and S.-Y. Lee, "Unpaired speech enhancement by acoustic and adversarial supervision for speech recognition," *IEEE Signal Process. Lett.*, vol. 26, no. 1, pp. 159–163, Jan. 2019, doi: [10.1109/LSP.2018.2880285](https://doi.org/10.1109/LSP.2018.2880285).
- [26] L. Yuan and X. Xu, "Adaptive image edge detection algorithm based on canny operator," in *Proc. 4th Int. Conf. Adv. Inf. Technol. Sensor Appl. (AITS)*. Harbin, China: IEEE, Aug. 2015, pp. 28–31.
- [27] S. Liu, L. Zhang, L. Fan, and X. Sheng, "An improved ray casting method for rendering radial anterior segment optical coherence tomography images," *J. Med. Imag. Health Inform.*, vol. 7, no. 5, pp. 944–948, Sep. 2017, doi: [10.1166/jmih.2017.2120](https://doi.org/10.1166/jmih.2017.2120).
- [28] D. Yin and R.-W. Lu, "A method of breast tumour MRI segmentation and 3D reconstruction," in *Proc. 7th Int. Conf. Inf. Technol. Med. Edu. (ITME)*. Huangshan, China: IEEE, Nov. 2015, pp. 23–26.
- [29] G. Pizaine, E. D. Angelini, I. Bloch, and S. Makram-Ebeid, "Vessel geometry modeling and segmentation using convolution surfaces and an implicit medial axis," in *Proc. IEEE Int. Symp. Biomed. Imaging: From Nano to Macro*, Chicago, IL, USA, Mar. 2011, pp. 1421–1424.
- [30] X. Li and M. T. Orchard, "New edge-directed interpolation," *IEEE Trans. Image Process.*, vol. 10, no. 10, pp. 1521–1527, Oct. 2001, doi: [10.1109/83.951537](https://doi.org/10.1109/83.951537).
- [31] X. Chen, J. Hwang, C. Lee, and S. Chen, "A near optimal QoE-driven power allocation scheme for scalable video transmissions over MIMO systems," *IEEE J. Sel. Topics Signal Process.*, vol. 9, no. 1, pp. 70–88, Feb. 2015, doi: [10.1109/STSP.2014.2336603](https://doi.org/10.1109/STSP.2014.2336603).
- [32] K. H. B. Voo and D. B. L. Bong, "Quality assessment of stereoscopic image by 3D structural similarity," *Multimedia Tools Appl.*, vol. 77, no. 2, pp. 2313–2332, Jan. 2018, doi: [10.1007/s11042-017-4361-2](https://doi.org/10.1007/s11042-017-4361-2).
- [33] H.-A. Li, M. Zhang, K. Yu, X. Qi, Q. Hua, and Y. Zhu, "R3MR: Region growing based 3D mesh reconstruction for big data platform," *IEEE Access*, vol. 8, pp. 91740–91750, 2020.
- [34] X. Zhou, W. Liang, K. I.-K. Wang, and S. Shimizu, "Multi-modality behavioral influence analysis for personalized recommendations in health social media environment," *IEEE Trans. Comput. Social Syst.*, vol. 6, no. 5, pp. 888–897, Oct. 2019, doi: [10.1109/TCSS.2019.2918285](https://doi.org/10.1109/TCSS.2019.2918285).



JING ZHANG was born in Xi'an, Shaanxi, China, in 1988. She received the B.S. degree from the Mathematics Department, Northwest University, Shaanxi, in 2010, and the M.S. and Ph.D. degrees in computer science and technology from Northwest University, in 2013 and 2018, respectively.

From 2018 to 2019, she was a Lecturer with the Xi'an University of Science and Technology, Shaanxi. She has been conducting one NSFC Project and one Project from the Shaanxi Science and Technology Department. She has been published eight articles in SCI and EI journal. Her research interests include the image processing and 3D reconstruction techniques, and fundamental study of signal processing and signal imaging.



LING-RUI GONG was born in Baoji, Shaanxi, China, in 1996. She received the B.S. degree in electronic information science and technology from Northwest University, in 2018, where she is currently pursuing the M.S. degree in communication and information system.

From 2018 to 2020, she has focused on the research in computer vision. Her research interests include dehazing, super-resolution, and deblurring of images.



KEPING YU (Member, IEEE) received the M.E. and Ph.D. degrees from the Graduate School of Global Information and Telecommunication Studies, Waseda University, Tokyo, Japan, in 2012 and 2016, respectively.

He was a Research Associate and a Junior Researcher with the Global Information and Telecommunication Institute, Waseda University, from 2015 to 2019 and 2019 to 2020, respectively, where he is currently a Researcher. He has hosted

and participated in more than ten projects, is involved in many standardization activities organized by ITU-T and ICNRG of IRTEF, and has contributed to ITU-T Standards Y.3071 and Supplement 35. His research interests include smart grids, information-centric networking, the Internet of Things, blockchain, and information security. He has served as a TPC Member for more than ten international conferences, including ITU Kaleidoscope, the IEEE Vehicular Technology Conference (VTC), the IEEE Consumer Communications and Networking Conference (CCNC), and the IEEE Wireless Communications and Networking Conference (WCNC). He was the Chair of the IEEE/CIC ICC 2nd EBTSRA workshop, the General Co-Chair and the Publicity Co-Chair of the IEEE VTC2020-Spring EBTSRA workshop, the TPC Co-Chair of the SCML2020, the Local Chair of the MONAMI 2020, the Session Co-Chair of the CcS2020, and the Session Chair of the ITU Kaleidoscope 2016. He has been a Lead Guest Editor of *Sensors*, *Peer-to-Peer Networking and Applications*, and *Energies*. He is an Editorial Board Member of the IEEE OPEN JOURNAL OF VEHICULAR TECHNOLOGY (OJVT).



XIN QI (Member, IEEE) received the M.E. and Ph.D. degrees from Waseda University, Tokyo, Japan, in 2016 and 2019, respectively. He is currently a Research Associate with the Global Information and Telecommunication Institute, Waseda University. His research interests include ICN and 3N for next-generation communication systems.



ZHENG WEN (Member, IEEE) received the B.E. degree in computer science and technology from Wuhan University, China, in 2009, and the M.Sc. and Ph.D. degrees from Waseda University, Tokyo, Japan, in 2015 and 2019, respectively. He became a Research Associate at Waseda University, in 2018, where he is currently an Assistant Professor (Lecturer) with the Department of Communication and Computer Engineering. His research interests include ICN/CCN for

next-generation communication systems, AI, and the IoT.



QIAOZHI HUA received the B.E. degree in electrical communication from the Wuhan University of Science and Technology, in 2011, and the M.S. and Ph.D. degrees from Waseda University, in 2015 and 2019, respectively. He is currently a Lecturer with the Computer School, Hubei University of Arts and Science, Hubei, China. His research interests include game theory and wireless communication.



SAN HLAING MYINT received the B.C.Tech., B.C.Tech. (Hons.), and M.C.Tech. degrees from the University of Computer Studies at Mandalay, Myanmar, in 2004, 2005, and 2008, respectively, and the Ph.D. degree from Waseda University, Tokyo, Japan, in 2019. He was a Tutor with the Ministry of Science and Technology, Myanmar, from 2007 to 2015. From 2009 to 2014, he was with the University of Computer Studies at Yangon, Myanmar, where he performed research

focused on sustainable cloud computing. He is currently a Research Associate with the Global Information and Telecommunication Institute, Waseda University. His current research interests include fifth-generation wireless networks and the analysis of channel coding methods.

...